67th International Astronautical Congress (IAC), Guadalajara, Mexico, 26-30 September 2016.

IAC-16-C1,9,4,x32785

A Concept for Capturing and Docking Spacecraft with Flux-Pinned Interfaces

Frances Zhu[a]*, Laura Jones-Wilson[b], Mason A. Peck[c]

[a] *Department of Mechanical and Aerospace Engineering, Cornell University, Upson Hall, Ithaca, NY, USA*, fz55@cornell.edu
[b] *Guidance and Control Systems Engineer, NASA Jet Propulsion Laboratory, 4800 Oak Grove Drive, Pasadena, CA,USA* Laura.L.Jones@jpl.nasa.gov
[c] *Department of Mechanical and Aerospace Engineering, Cornell University, Upson Hall, Ithaca, NY, USA*, mp336@cornell.edu
* Corresponding Author

Abstract

Flux-pinned interfaces for spacecraft leverage the physics of magnetic flux pinning to govern the dynamics between close-proximity spacecraft. The behavior of this interface enables a magnet to be held at a distance in up to six degrees of freedom relative to a type-II superconductor without contact or active control systems. This behavior is the result of a magnetic potential well with an equilibrium set by designer of the interface. When applied to a conceptual sample capture scenario, this approach offers several unique advantages over traditional mechanical capture systems, including robustness to control failures and the ability to preferentially orient the capture target without mechanical keying features. However, as a passive system, it is important to characterize the depth and shape of the potential well in order to bound the acceptable relative motion between a notional spacecraft and a notional sample cache to ensure a successful capture. This paper presents the results of a series of air bearing experiments designed to determine these bounds. Extrapolating from the ground testing environment, it was determined that the FPI is expected to work at a range of 50 cm in orbit around Mars, and operates best in a path angle of 0 degrees. It can tolerate a total relative translational velocity of up to 4.7 cm/sec or a total angular rate of 24 deg/sec between a spacecraft and a sample cache.

Keywords: spacecraft, flux pinning, sample return, experiments

Nomenclature

α Path angle
ϕ Yaw angle
r Translational radial displacement
θ Roll angle

Acronyms/Abbreviations

Degrees of Freedom (DOF)
Fast Fourier Transform (FFT)
Flux-Pinned Interface (FPI)
Flux Pinned interface for Orbiting Sample capture (FPOS)
Inertial Measuring Unit (IMU)
Orbiting Sample (OS)
Orbiting Sample Analogue (OSA)
Sample Return Orbiter (SRO)
Sample Return Orbiter Analogue (SROA)
Yttrium Barium Copper Oxide (YBCO)

1. Introduction

CLOSE-PROXIMITY spacecraft operations – such as rendezvous, docking, or grappling – are critical capabilities for a variety of mission concepts of great interest to the spacecraft dynamics community, including on-orbit servicing or assembly, missions requiring a transfer of material or people from one spacecraft to another, and potential sample capture. These maneuvers are often implemented in phases, separated by the range of the different sensors used to perform each phase. Although all phases of these maneuvers carry an inherent amount complexity, the phase fraught with the most risk would be the final approach, where the spacecraft would close the last meter between them. Most techniques to perform this final approach would rely on active control and mechanical features, with their associated set of advantages and risks. This work instead studies a relatively new technology known as a flux-pinned interface (FPI) for spacecraft as an alternative to these traditional solutions. FPIs use the phenomenon of magnetic flux pinning [1], [2], [3] – an interaction between type-II superconductors and magnetic fields – to manipulate the behavior between two spacecraft. This effect is more widely known for its application to Maglev trains or frictionless bearings, but because it exhibits passively stable dynamics in up to six degrees of freedom (DOF), it has interesting implications for use in close-proximity spacecraft maneuvers.

Over the past decade, FPIs have been studied for use in formation flying [4], autonomous assembly [5], magnetic kinematic mechanisms for spacecraft deployments [6], and docking interface augmentation [7]. Research both in laboratory [8], [9], and microgravity environments [10] have led to a broad understanding of the design principles that govern this technology as well as its expected performance under a variety of

circumstances. This paper extends that groundwork to the properties of a specific FPI designed to support a conceptual sample capture operation. In particular, it will explain the background on flux-pinned interfaces and the specific scenario and FPI design being studied in this work. Then, we explain the specific air bearing test campaign objectives and design as well as the testbed hardware used to conduct the experiments. The results from these experiments are then explained in the subsequent section, especially as they relate to the sphere of influence, stiffness and damping of the interface, and capture threshold offered by this FPI design. The paper concludes with an assessment of the implications for a sample-capture mission concept using an FPI and recommendations on future work to address some of the questions raised by the results.

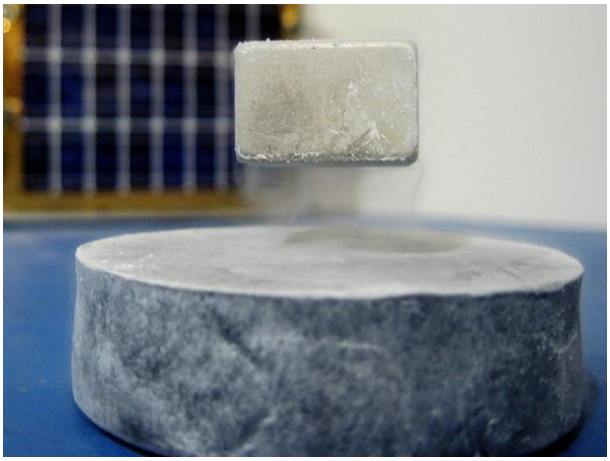

Figure 1. A flux-pinned system with a magnet (top) levitated over a type-II superconductor disk (bottom).

2. Flux-Pinned Interfaces and Notional Sample Capture

2.1. Magnetic Flux Pinning and FPIs

Magnetic flux pinning is a unique property of type-II superconductors where magnetic flux lines can become "pinned" inside the volume of the superconductor, causing the source of the magnetic field to maintain its position and orientation relative to the superconductor. This equilibrium is set by the magnetic flux configuration inside the volume of the superconductor at the point it crossed below its material-dependent critical temperature in a process known as field cooling. The magnetic field penetrates the unique structure of the superconducting disk and as the material around the magnetic field becomes superconducting, supercurrent vortices are generated around those field lines. These vortices then resist changes in magnetic flux via Lentz's Law, which causes the superconductor to apply – via these vortices – forces and torques that maintain the relative equilibrium between the magnetic field source and the superconductor. Thus, as shown with the Yttrium Barium Copper Oxide (YBCO) superconducting disk in Figure 1, if a magnet is located relative to a superconductor as the superconductor is cooled below its critical temperature (in this case, 88K), the superconductor acts to maintain the equilibrium, even levitating the magnet against gravity. This effect lasts until the material is allowed to warm above its critical temperature, where it gains internal resistance that causes the supercurrent vortices to dissipate.

Flux pinning has a number of properties that make it particularly interesting for relative-motion control and space applications. Most importantly, the equilibrium generated by a flux-pinned system is passively stable in up to six degrees of freedom and can be controlled by changing the magnetic field in the system [11]. The equilibrium can be set by the configuration of the system during the field-cooling process, and can be selected to impart a given separation distance between two bodies. This combination of traits means that a flux-pinned system can effect change on the relative state between two bodies without contact between them. The magnetic potential well formed by flux pinning can result in behavior similar to that implemented by a non-linear spring whose influence drop of as roughly as distance to the fourth power. This system can thus act to correct misalignments between close-proximity bodies and resist motion that may cause impacts or collisions between them, making it particularly interesting for sample capture applications.

For space applications, a flux-pinned interface (FPI) typically involves superconductors on one spacecraft and an array of magnets on the other. Thus, when these bodies are in close proximity, the physics of flux pinning can dominate the relative motion between them, providing passive impact attenuation, misalignment correction, and a connection with a tunable stiffness and equilibrium distance. Although a number of applications have been considered in previous studies [12], [13], [14], [15], [16], this work considers the design and performance of an FPI developed specifically to perform a sample capture / docking activity.

2.2. Comparison to Alternative Capture Solutions

Most autonomous docking techniques use either a mechanism (such as a robotic arm), or actuators attached to the main spacecraft to close the final distance between spacecraft [17], often in conjunction with a mechanical capture cone or locking feature to secure the final mate [18]. Other studies have examined the use of magnetic docking solutions that use actively controlled magnets to augment (or completely control) the docking sequence [19]. None of these techniques can generate the passive equilibrium in six degrees of freedom that FPIs offer, and all of them ultimately require some kind of contact between the bodies to work. Any abrupt mechanical

contact between a notional return vehicle to earth and a spacecraft contaminated with surface material could bring a measure of uncertainty and risk into the sequence. Furthermore, these traditional docking solutions are often dependent on lighting conditions or other sensor conditioning, and are vulnerable to errors in the control system. FPIs, are based on passive physics, so the interfaces are robust to these kinds of risk. The interface can be solid-state, for example, and does not require the use of sensors at all once the two spacecraft are within the FPI effective range.

Finally, if a specific orientation is required for the mate, many traditional solutions require mechanical keying features on the target surface and mechanisms to achieve this state. Because an FPI acts on magnetic field shape, rather than mechanical shape, it is possible to design an FPI that is independent of the mechanical configuration of the target. Once the capture and reorientation is complete, the interaction can be removed by warming the superconductors, simplifying subsequent maneuvers.

In addition to these advantages, FPIs also carry a unique set of risks. In particular, for potential sample capture applications, exposure to magnetic fields can adversely impact the sample science, so additional shielding would be necessary to avoid this exposure. Also, FPIs require a proper field-cooling configuration to set up the interface for capture- this critical event introduces a set of risks that must be addressed (albeit prior to the capture phase itself). Similarly, thermal failures can lead to the loss of the interaction, and docking scenarios with significant amounts of energy may not stay within the potential well and not make a successful capture on the first attempt. These risks must be understood and addressed in the FPI technology development efforts for docking and potential sample capture applications if the technology is ever to become a viable alternative to other more traditional solutions.

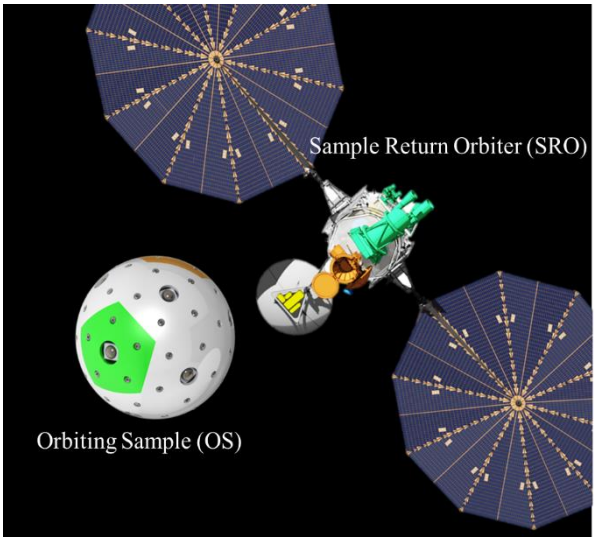

Figure 2. A conceptual sample-capture flux-pinned interface, where an orbiting sample containing a sample cache and populated with surface permanent magnets must be collected by a sample return orbiter containing field-cooled superconductors and electromagnets.

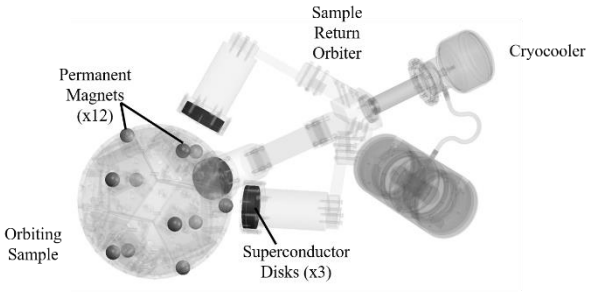

Figure 3. An FPI design for a sample capture concept where a cryocooler maintains three superconductors below their critical temperature so that they can capture an OS prepared with permanent magnets.

2.3. Sample Capture and FPI Design Concept

In order to understand the FPI design considered in this work, it is first necessary to understand the sample capture scenario concept under consideration. In this concept, shown in Figure 2, a cache of planetary samples is already in orbit around its source body. Although many different concepts exist for the size, shape, and other properties of this cache (called an orbiting sample, or OS), for the purposes of this study, the OS is a small, passive sphere with a diameter of approximately 20 cm and a mass of less than 6 kg. Because it does not contain its own propulsive or maneuvering capabilities, the OS must be captured, stabilized, and manipulated into an appropriate orientation by a sample return orbiter (SRO) for the return trip to Earth. For the purposes of this study, the SRO is considered a large (> 1000 kg, ~10 meters in body length) spacecraft with the full set of maneuvering capabilities, thermal control, and other resources available to traditional spacecraft.

The highly capable SRO, when outfitted with an FPI, would cool down the superconductors as it approaches the OS orbit prior to capture operations, using surrogate training magnets to generate the appropriate field-cooled equilibrium. This set of magnets can be jettisoned or removed via mechanism once the cooling process is complete. Once properly configured, the SRO then navigates to within range of the FPI, where the OS will be drawn into its passively stable, non-contacting equilibrium. This soft-capture maneuver can benefit from the misalignment correction and impact attenuation properties offered by an FPI. Similarly, once captured, the OS can be reoriented using electromagnets to support cleaning or containment operations and to achieve the proper ingestion orientation, all without contacting the SRO. Once the OS is ingested into the SRO, the purpose

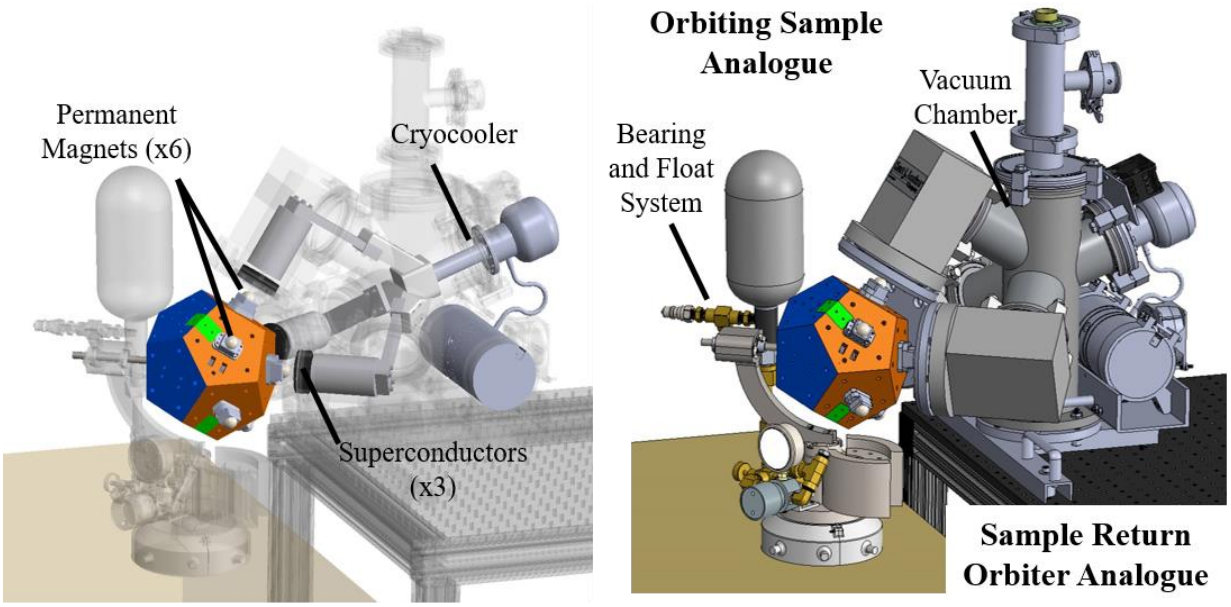

Figure 4. The key elements of the FPOS testbed, including elements that would be present in an orbital system (left), and elements included in order to support testing in a ground environment (right). Both analogues are based on conceptual mission hardware.

of the FPI is complete and the thermal control of the superconductors can be powered off.

In order to achieve these objectives, the OS's surface is populated with an array of spherical 1.9 cm diameter Neodymium permanent magnets, placed evenly on the points of a dodecahedron with the magnetic dipoles all facing radially outward, as shown in Figure 3. This configuration ensures that each plane of the OS is identical to the next, enabling the system to use the same field-cooled superconductors to capture any given face. Similarly, this design enables the system to achieve an orientation where any plane is facing the SRO, to ensure that all faces of the OS can be cleaned and the system can be ingested in the proper orientation.

The other half of the interface, mounted to the SRO, contains an array of three single-grain YBCO superconductor disks 1.6 cm high and 5.6 cm in diameter. The superconductor YBCO was selected because of its relatively high critical temperature of 88K (making it easily achievable in laboratory conditions) and its well-characterized flux pinning behavior. This material also exhibits flux pinning effects across a large range of magnetic field strengths, making it particularly tailorable to many applications. These particular disks were selected because of their low propensity for hysteresis and their commercial availability. Other superconductor types or disk sizes may be optimal for this particular application and should be studied in future work.

Each of these disks are mounted such that one magnet can be centered over it at the equilibrium with a separation distance between the surface of the superconductor and the closest tangent point on the magnet of 1.5 cm. The planes of each superconductor disk are parallel to three adjacent planes on the OS dodecahedron mounting surface, as shown in Figure 3. This superconductor arrangement provides redundancy, greater capture stiffness due to the three interfaces (to avoid OS-SRO collisions), and clocking stiffness to maintain a stable equilibrium between the OS and SRO in all six degrees of freedom.

3. Experimental Setup

3.1 Test Campaign Objectives

In order to raise the technology readiness level of FPIs for sample capture, it is important to characterize the size and shape of the potential well that is formed by the field-cooled superconductors. This information provides the bounds on acceptable relative states (position, orientation, and linear/angular velocities) between an SRO and OS to ensure the FPI can generate a successful capture. Thus, the flux-pinned interface for orbiting sample capture (FPOS) air-bearing testbed (shown in Figure 4) was created in order to directly measure these values, in addition to improving FPI modeling capabilities and establishing the reliability of ground test environments in evaluating these parameters for an FPI.

3.2 Testbed Hardware Description

The FPOS testbed is four degree of freedom system – designed to improve on Cornell's FOURTE testbed [20]– that uses a mechanical bearing mounted to a planar

air bearing in order to simulate the motion of spacecraft under the influence of an FPI for sample capture. The testbed has two primary elements: the Orbiting Sample Analogue (OSA) and the Sample Return Orbiter Analogue (SROA), which are based on conceptual mission hardware. The OSA is a 1:1 scale of a conceptual OS (20.3 cm in diameter) that is mounted to a bearing and float system that provides two translational and two rotational degrees of freedom (shown in Figure 5.). In order to ensure that the OSA can rotate freely on the mechanical spindle, only six of the permanent magnets are included on the icosahedron pattern, but the distance and relatively sharp decrease in influence as a function of distance suggests that this approximation should not have a significant effect on the field-cooled equilibrium interacting with the FPI. Although the OS interior will contain surface samples, the OSA has an avionics and sensor package (which includes an Epson M-G362 inertial measuring unit (IMU)) to aid in modeling the dynamics on the testbed. The IMU sampled at 125 Hz with a dynamic range up to 150 deg/s and 3g with 32 bit resolution. This sensor package communicates with the testbed laptop via WiFi. The rotating sphere of the OSA is also prepared with markers identifiable by the testbed Vicon position sensor system.

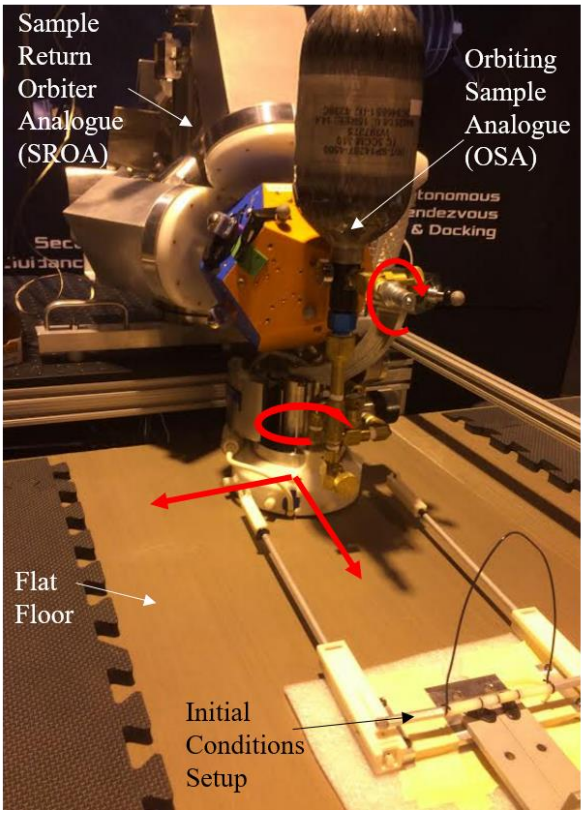

Figure 5. The major components of the FPOS testbed used to generate the results discussed in this work.

The SROA, on the other hand, is stationary and includes the relevant flight-traceable thermal systems and three YBCO superconductor disks necessary to support the sample capture FPI design. The thermal design and modeling for this unit, which includes a vacuum chamber that surrounds the superconductor disks in order to support ground testing in an ambient thermal environment is described by McKinley [21]. The significantly larger mass of the SRO relative to the OS means that a stationary SROA is a reasonable approximation of the dynamics of the flight system. The SROA is also outfitted with thermal sensors to monitor the temperature of the superconducting disks and Vicon markers to provide a stationary point of reference in the data processing.

In addition to these main elements, the testbed also includes a Vicon sensor system, a laptop that collects the video, Vicon data, and initializes the wireless avionics package on the OSA, a mechanism for imparting initial conditions on the OSA, and a leveled flat floor for performing the experiments. These elements are shown in the photograph in **Figure 5.** and the schematic shown in **Figure 6.** The Vicon sensor system includes 5 Bonita cameras and Tracker 1.3.1 software. The cameras and tracking system resolve position to within 0.2 mm with an approximate (but varying) update rate of 100 Hz. The initial conditions setup is a set of spring-loaded arms (known as the horseshoe) mechanically attached to the SROA that can be adjusted to provide either stationary OSA initial conditions (static position or orientation relative to the SROA) or can be compressed and released to impart translational or angular momentum to the OSA. Finally, the FPOS testbed utilizes the JPL Formation Control Testbed (FCT) flat floor to leverage its finely leveled surface to minimize gravity bias and friction [21]. The flat floor is polished to within a thousandth of an inch across each panel and flattened with a state of the art metrology system.

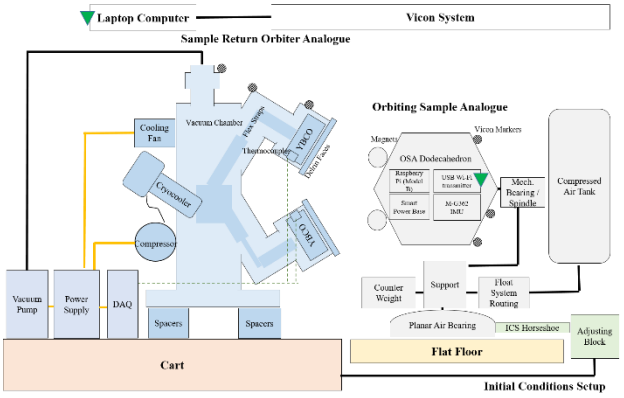

Figure 6. A schematic of the FPOS testbed elements.

Table 1. Physical Parameters for the FPOS Testbed

Physical Parameter	Value	Units
OSA Mass	14.23	kg
Inertia about spindle	0.0044	kg m^2
Inertia about air bearing	0.062	kg m^2
Coefficient of kinetic friction in ball bearing	0.0023	--
Coefficient of kinetic friction between air bearing and floor	0.0019 L 0.0027 T	--
Center of rotation displacement along spindle	-7.27	mm
Center of rotation displacement away from spindle	-1.18	mm

3.3 System Dynamical and Mass Properties

In order to model the OSA behavior, it is necessary to determine the mass properties of the unit and the forces acting on it beyond those generated by the FPI. The OSA has a diameter of 20.3 cm and a mass of 14.23 kg. The moment of inertia of the rotating dodecahedron assembly about the mechanical bearing/spindle is 0.0044 kg m^2 and the moment of inertia about the whole assembly is 0.062 kg m^2 about the axis perpendicular to the flat floor.

The offset between the center of rotation and center of mass of the system causes torques to arise from the FPI forces acting on the OSA. Off-axis center of mass locations can also cause uneven loading of the bearing which can also adversely affect the dynamics. In order to counteract these effects, the OSA was designed to have a center of mass as close as possible to the axis of rotation, and small trim masses were added on the dodecahedron assembly until the rotating assembly did not exhibit any observable pendulum effects about its mechanical spindle. According to the CAD file, the offset of the center of mass of the dodecahedron assembly was -1.18 mm from the shaft, and was -7.27 mm from the system center of mass along the shaft in the direction of the dodecahedron assembly, refer to figure Figure 7. During characterization testing, it was discovered that the center of mass offset of the system from the geometric center of the air bearing led to increased friction between the air bearing and the flat floor, so the OSA was redesigned to its present form to bring the center of mass to within 10 mm of the air bearing's center.

Although designed to have limited impact on the dynamics, the mechanical and air bearings in the OSA inevitable do enact some dissipative forces on the assembly. The empirically determined kinetic coefficient of friction for the OSA mechanical bearing has an average of 0.0023 with a standard deviation of 2.4e-4. [20] Air bearings also exhibit dissipation in the form of shear forces of the air between a moving plate and the static flat

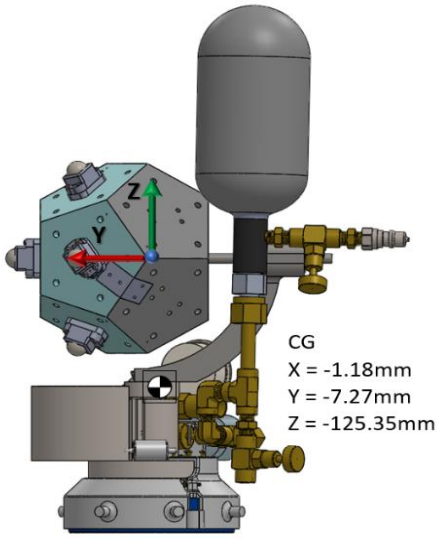

Figure 7. Center of mass for the OSA relative to the geometric center of the dodecahedron assembly (shown at the origin of the coordinate axes).

floor. The dissipative coefficient experimentally determined on this floor with a similar set of air bearings was established to be 0.0027 in the transverse direction (away from the SROA) and 0.0019 in the lateral direction (along the face of the SROA) [23]. The unique weave in the flat floor construction and the relatively low float height of these air bearings contributes to the directionality in the results. Air drag is considered negligible in this analysis.

3.4 Experiment Operation

With this hardware, a series of tests were carried out over the summer of 2016 in order to establish the FPI's sphere of influence, stiffness and damping, and capture energy threshold. Prior to every test campaign, the vacuum chamber was evacuated (a process that took

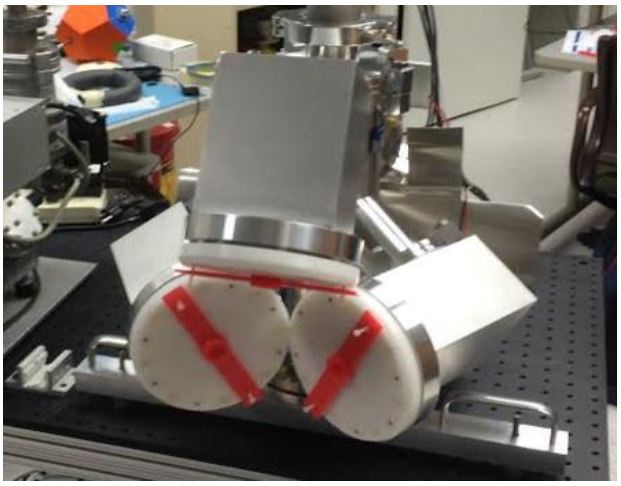

Figure 8. Magnet spacers mounted to the SROA delrin faces in the location for field-cooling (magnets not shown).

approximately 12 hours), and then the cryocooler was powered on to cool the superconductors from ambient temperature to 80 K (a process which took another 12 hours). During this cooling process, the superconductors were field-cooled with surrogate magnets temporarily mounted to the SROA face with plastic spacers as shown in Figure 8. The equilibrium was set where a magnet is centered 1.5 cm directly above the center of each superconductor disk. With the inclusion of the delrin faces and other material between the superconductor disks and the magnets on the OSA, the available gap before an impact is 0.8 cm. These field-cooled positions were selected based on prior experience to achieve a reasonable compromise between stiffness of the interface and impact likelihood. The FPI can be re-optimized for different field-cooling configurations if necessitated by the particular concerns of the mission scenario.

Once the superconductors were below their critical temperature, the plastic spacers were removed and the OSA was placed onto the flat floor and allowed to settle into an equilibrium with the SROA. This equilibrium was recorded by the Vicon system for later processing. The OSA was then pulled away from the equilibrium and rotated abruptly about its spindle in order to provide a timestamp-syncing maneuver distinguishable by the IMU and the Vicon system. The system was then placed at the appropriate initial conditions for the test, and three trials with the same initial conditions were recorded. The field-cooling solution was re-imprinted only four times throughout the test campaigns described here. Once the set of tests was complete, the data from the IMU was downloaded from the onboard card and processed to sync the timestamps with the Vicon system. These measurements were blended using a moving average filter to establish the estimated state of the OSA. The accelerometer values were processed with a thresholding algorithm, and any time during the experiment where the IMU recorded a spike, it was evaluated as a strike between the OSA and SROA.

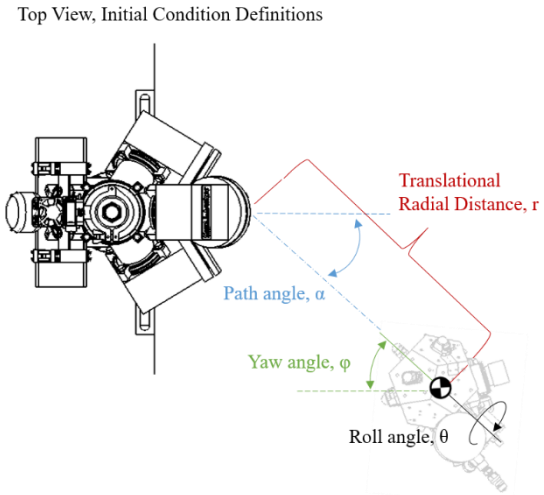

Figure 9. Schematic of the initial condition parameters under test, where zero corresponds to the initial conditions and the positive angle is shown.

3.5 Experiment Types

There are five different types of tests discussed in this work: sphere of influence, roll stiffness and damping, natural mode, capture, and tumble. The primary test suite consists of the data collected when the OSA had 4 degrees of freedom (with the exception of the roll stiffness and damping tests, which only had one DOF). Some of these tests were also repeated in a DOF comparison suite where the roll degree of freedom about the spindle was locked out to understand the sensitivity

Table 2. Experiment Initial Conditions and Configuration

	Primary Test Suite					Constrained DOF Comparison Test Suite			
Test Name	**Sphere of Influence Tests**	**Roll Stiffness and Damping Tests**	**Natural Mode Tests**	**Capture Tests**	**Tumble Tests**	**Sphere of Influence Tests**	**Natural Mode Tests**	**Capture Tests**	**Tumble Tests**
# Total Experiments Performed	120	72	180	105	180	40	12	50	70
# Trials for Each Initial Condition	3	9	3	3	3	1	1	2	2
# DOF	4	1	4	4	4	3	3	3	3
Translational Radial Distance from Equilibrium, r (cm)	1, 2, 4, 6, 8, 10, 12, 14	0	0, 1, 2	18	18	1, 2, 4, 6, 8, 10, 12, 14	0, 1, 2	18	18
Initial Path Angle (Angle Relative to Perpendicular Approach of Equilibrium), α (deg)	0, 5, 10, 15, 30	--	0	0, 5,10, 15, 30	0, 5,10, 15, 30	0, 5, 10, 15, 30	0	0, 5, 10, 15, 30	0, 5, 10, 15, 30
Initial Roll Angle (Rotation about Spindle), θ (deg)	0	5, 10, 15, 30	5, 10, 15, 30 (varied with 0 deg yaw)	0	0	0	0	0	0
Initial Yaw Angle (Rotation about Planar Air Bearing), φ (deg)	oriented to point to equilibrium, matched with path angle (0, 5, 10, 15, 30)	0	5, 10, 15, 30 (varied with 0 deg roll)	oriented to point to equilibrium, matched with path angle (0, 5, 10, 15, 30)	45 when <= 20 deg/s yaw angular velocity, 90 when > 20 deg/s yaw angular velocity	oriented to point to equilibrium, matched with path angle (0, 5, 10, 15, 30)	5, 10, 15, 30	oriented to point to equilibrium, matched with path angle (0, 5, 10, 15, 30)	45 when <= 20 deg/s yaw angular velocity, 90 when > 20 deg/s yaw angular velocity
Initial Translational Velocity, $\dot{r}$ (cm/s)	0	0	0	1, 2, 3, 4, 6, 8, 10	0.5, 1, 1.5, 2, 2.5, 3, 4, 5 (coupled to yaw angular velocities)	0	0	1, 2, 3, 4, 5	1, 2, 3, 4 (coupled 1:1 to yaw angular velocity, where higher translational velocities match higher yaw angular velocities)
Initial Angular Velocity About Roll $\dot{\theta}$ (deg/s)	0	0	0	0	0	--	--	--	--
Initial Angular Velocity About Yaw, $\dot{\Phi}$ (deg/s)	0	0	0	0	5,10,15,20,25,30 (coupled to translational velocities)	0	0	0	6, 12, 18, 24 (coupled 1:1 to initial translational velocity, where higher yaw angular velocities match higher translational velocities)

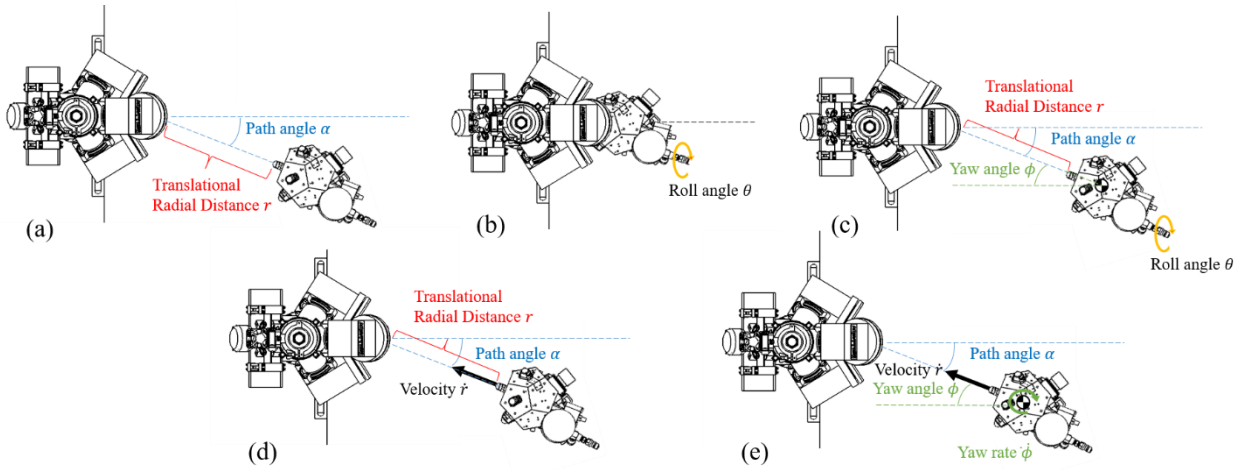

Figure 10: From the top left to bottom right, top-down views of the a) sphere of influence test b) roll stiffness and damping test, c) natural modes test, d) capture test, and e) tumble test

of the FPI to these non-flight-like constraints. The initial conditions and number of trials for each one of these experiments is shown in Table 2, and the parameters that were varied over the different runs are defined in the schematic in Figure 9.

The sphere of influence tests are designed to understand how far away the FPI influence can be used to pull the OSA into the potential well on this testbed. This information also provides insight into passive dynamics (such as the differences in capture time) for different capture distances and angles. This experiment, shown in Figure 10a, varied the path angle and translational displacement from the equilibrium, then released the OSA from a static state. The passive dynamics of the FPI captured the OSA if the environmental effects did not overwhelm the attractive forces from the FPI. The experiments were ended if the OSA exhibited no noticeable motion toward the SROA after 15 seconds, which may conservatively truncate the measured influence range.

The roll stiffness and damping tests in Figure 10b aim to determine if the advanced frozen image model [24] can be applied to this FPI to assess roll stiffness, and to provide an empirical estimate for damping, which the model does not predict. The Kordyuk model predicts flux-pinning dynamics normal to the surface of the superconductor, but the lateral and rotational dynamics are not as well characterized. Thus, in order to understand the full 4 DOF rigid body dynamics, these tests only left the roll degree of freedom unconstrained, with the system otherwise in its equilibrium. The OSA was then perturbed at different roll angles, and allowed to naturally settle. Two different relative equilibria were tested (two different magnet trios 72 degrees apart) to investigate consistency across relative equilibria.

Natural mode experiments, shown in Figure 10c, investigate the coupling effects of rotation on translational dynamics. By perturbing all degrees of freedom available to the experiment testbed, natural modes and frequencies are excited. These modes and frequencies are important in characterizing the stiffness and damping of the flux pinned interactions. In this experiment, every degree of freedom is displaced from the equilibrium position or orientation and held stationary, then released from a static state. The full 4 DOF system testing examined the angular displacement about each axis separately.

Capture experiments, in Figure 10d, mimic a capture maneuver within the 4 DOF constraints of the testbed. In this type of test, the OSA is launched at the stationary SROA with a specified initial velocity. These tests vary the initial translational velocity but do not include any angular velocity. The initial position is always 18 cm away in distance (because this is the distance on this testbed at which the FPI could not attract the OSA into the potential well without additional energy input). The entrance path angle was varied to test a cone of possible path angles. The ultimate goal of these experiments is to understand what kinetic energy thresholds generate capture successes.

The tumble experiments, shown in Figure 10e, build upon the capture experiments by adding angular velocity. This addition generates some of the most complicated dynamics but also simulates the most realistic flight scenarios. The OSA is launched at varying translational velocities, angular velocities, and path angles for the full 4 DOF. The yaw angular velocity and translational velocities are coupled due to the fact that the difference in compressed spring lengths counted in pegs. These experiments will directly inform us of the maximum capabilities of the flux pinned interface under more realistic dynamic conditions.

A subset of these tests were also conducted with the spindle locked in place, thus reducing the OSA dynamics

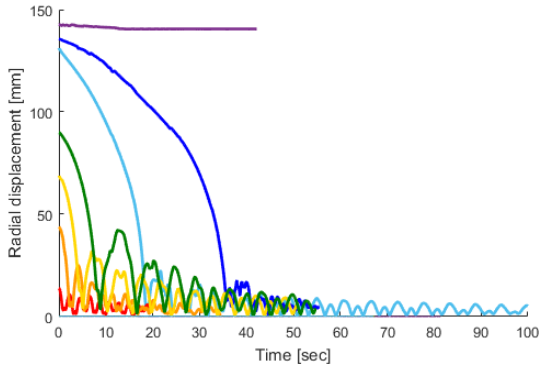

Figure 11. Time histories of radial displacement for different initial displacements, showing the dynamics of tests within the sphere of influence and a test that was not drawn in

to three degrees of freedom in order to evaluate how the results would change when fewer degrees of freedom were available to the system. The FPI's sensitivity to constrained degrees of freedom can be used guide decisions about the next steps in the technology development process.

4. Experimental Results

4.1 FPI Sphere of Influence and Passive Dynamics

The sphere of influence tests were designed to empirically determine the maximum range and shape of the potential well generated by the FPI in order to 1) evaluate where the attractive forces imparted by the FPI were overwhelmed by environmental factors of this particular testbed and 2) characterize the passive dynamics of the system at a range of initial conditions, as seen in Figure 11. As shown in Figure 12, the OSA reliably captured for a radial distance from the equilibrium of less than 12 cm in the 4DOF testbed but for distances past 14 cm, the OSA was very unlikely to capture. Thus, the radial range of influence for this FPI on the testbed was between those numbers. Using the frozen image and dipole model [24] [25] [26], the magnitude of the FPI-generated forces acting on the OSA at 12 cm from the equilibrium at 0 deg path angle is approximately 5 mN.

The data show no apparent trends as a function of initial path angle – the influence of the FPI appears to be a function of radial distance from equilibrium and independent of path angle up to 45 degrees. However, more data are needed to confirm this preliminary assessment, especially at smaller radial displacements.

When applied to a flight scenario, the sphere of influence of the same FPI is expected to be larger because the environmental forces that overwhelm the FPI attraction are significantly smaller. In LEO at 400 km altitude, for example, the dominant environmental force

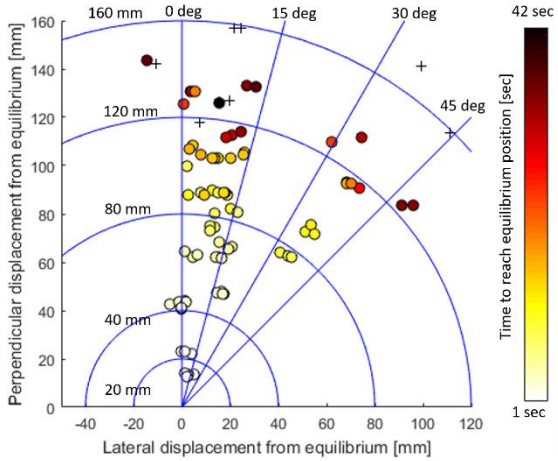

Figure 12. A plot of as-measured displacement from the equilibrium (shown at the origin) for both initial radial distances and path angles in the 4DOF sphere of influence tests. The heat map illustrates the travel time of the OSA until it first passes through equilibrium position.

is atmospheric drag assuming the system has no net magnetic dipole interacting with Earth's magnetic field. The orbital OS described previously would generate approximately 0.0055 mN of drag force under these conditions. The equivalent sphere of influence for the LEO threshold force is 26 cm. In a Mars orbit, on the other hand, the dominant environmental force is solar radiation pressure, which would generate a force of approximately 0.0001 mN on a 20.3 cm OS. The equivalent sphere of influence for the Mars orbit threshold force is therefore conservatively 50 cm, although the directionality of the forces is an important element that may extend the FPI range beyond this value.

4.2 FPI Roll Stiffness and Damping

The roll stiffness and damping tests were performed in order to empirically characterize the dynamic properties of the roll axis of the FPI as measured independently of all other degrees of freedom in the FPI.

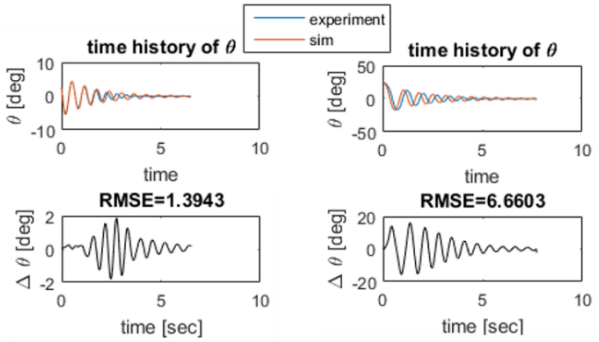

Figure 13: Time history and error between the time histories of a small angle (left) and large angle (right) displacement test, showing a comparison of the experiment vs simulation

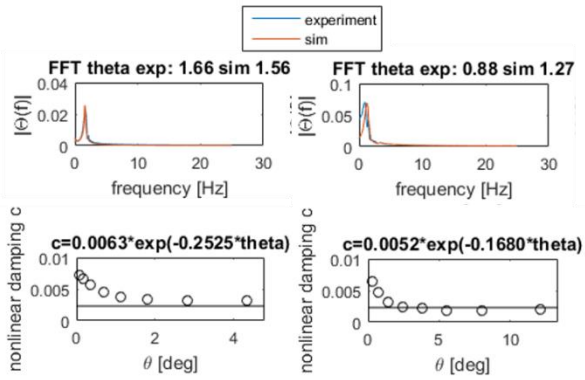

Figure 14: First row is a Fast Fourier transform of small angle and large angle displacement tests with nonlinear damping in the second row

The OSA under an angular displacement exhibits an underdamped oscillatory behavior, as shown in a representative trial with a small (5 deg) displacement in Figure 13 and a large (30 deg) displacement in Figure 14.

The motion of the OSA exhibits a natural frequency of about 1.66 Hz for small displacements (5 deg) and 0.88 Hz for large displacements (30 deg), when any nonlinearities are presumably more likely to be excited. The nonlinearity in the larger displacement experiments also smears the FFT peak across more frequencies, making the peak less distinct. This nonlinearity is much clearer when observing the peak frequency of the Fast Fourier Transform (FFT) plotted as a function of initial displacement roll angle for all of the trials, as shown in Figure 15. The figure shows that the fundamental frequency of the system can vary by as much as 0.6 Hz across the 30 degree initial condition spread.

The experimental data do not show a linear damping trend; rather, the damping coefficient calculated from each peak using logarithmic decrement shows that there is a clear dependence on angular displacement and/or angular velocity. The damping close to the equilibrium orientation or zero angular velocity has the highest damping, whereas the damping coefficient converges to the friction coefficient of the ball bearing (0.0023, shown as a line in the damping plot) as the magnet moves farther away from equilibrium. The FPI clearly exhibits additional damping beyond that produced by the friction in the bearing, which may be the effect of eddy current damping between the permanent magnets and the aluminium SROA structure. When the displacement is within a degree of the equilibrium, the damping appears to be over three times that which is seen at larger displacements.

When this interaction is modelled using the frozen image model [24] with an added nonlinear damping term that has been empirically determined by these tests, the equations of motion are:

$$\tau_{FP} = I\ddot{\theta} + c_1 e^{-c_2\dot{\theta}}\dot{\theta} \qquad (1)$$

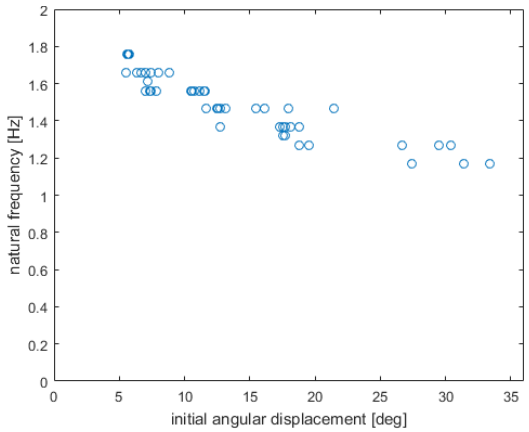

Figure 15. Dominant natural frequency is dependent on initial angular displacement due to nonlinear flux pinning interactions for 1 DOF experiments

These results are also plotted in Figure 13 and Figure 14. Clearly, the small angular displacement experiments better matched simulated dynamics; the natural frequency of the underdamped system was predicted to within 0.1 Hz (about 6% of the simulated value). The simulations of larger angular displacements (15 degrees and above), on the other hand, match the experimental data's general shape, but the natural frequencies differ by almost 0.4 Hz (or 30% of the simulated value). These results suggest that, even for this relatively simple, single-degree-of-freedom system, the damped advanced frozen image model can be used to evaluate natural frequencies at small displacements about the roll equilibrium, but larger displacements (where more of the nonlinearity is in effect) and any time history prediction will require modifications to the basic model to better match the observed motion.

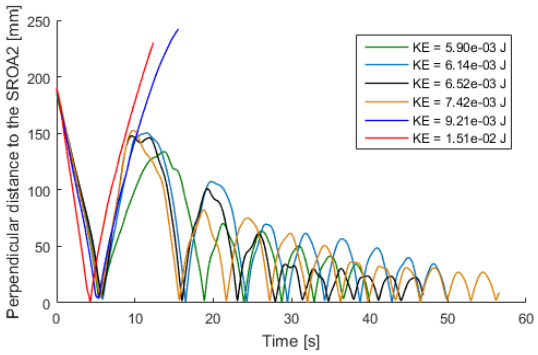

Figure 16: Time history of capture tests at 0 degrees with different initial kinetic energies

4.3 FPI Capture and Tumble Conditions

The sphere of influence tests examined the case when the potential energy well created by the field-cooled magnetic field in the superconductors draws in the

OSA from a state with no kinetic energy. The capture and tumble tests, on the other hand, were designed to characterize the bounds of rotational and translational kinetic energy that lead to capture, escape, and impacts in the FPI. If the kinetic energy of the OSA is larger than the potential well created by the FPI, the OSA will escape from the FPI (rather than being captured), as shown in Figure 16. Similarly, if the kinetic energy of the system can generate motion that exceeds the separation distance between the OSA and SROA, an impact will occur (which is undesirable for many sample capture scenarios). A capture without a collision is therefore the most desired sample capture outcome, and an escape with an impact is the least desired. These tests examined these kinetic energy thresholds.

The capture tests enter the potential energy well with only translational velocity. The OSA yaw angle matched the path angle when entering the sphere of influence to ensure that the potential energy well was stable (drawn in) vs. unstable (repulsed out), refer to Figure 17 and Figure 18. The tumble tests did not guarantee that the OSA entered the potential well with a stable orientation and also added rotational kinetic energy. In order to make the computation of the energy in the system more straightforward, the system was placed outside of the range of the FPI attraction (as established by the sphere of influence tests) and given an initial velocity to enter the FPI's potential well.

Figure 19 shows the capture tests as a function of their path angle, translational and angular velocity, and final impact/capture state. Figure 20 is a different view of the same scatter plot, but at a different perspective to highlight different observations. As expected, lower velocity tests capture more consistently than higher velocity tests, and the system will capture and impact before it escapes without an impact. Reliable captures

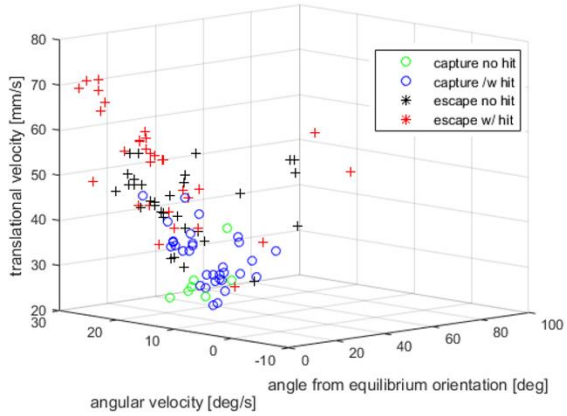

Figure 17. 3D scatter of 4 DOF tumble tests plot with varying absolute angles from equilibrium, entrance angular velocities, and translational velocities

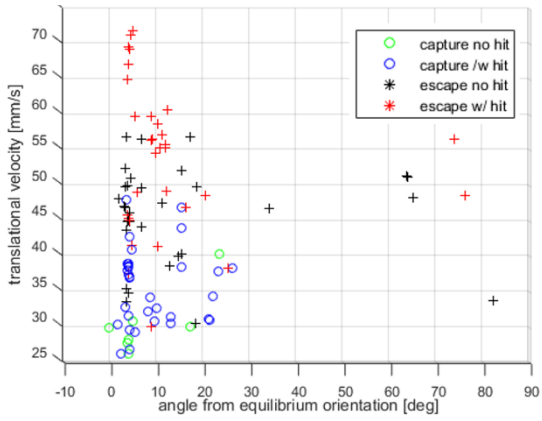

Figure 18. Scatter plot of 4DOF tumble tests with varying absolute angles from equilibrium and entrance angular velocities

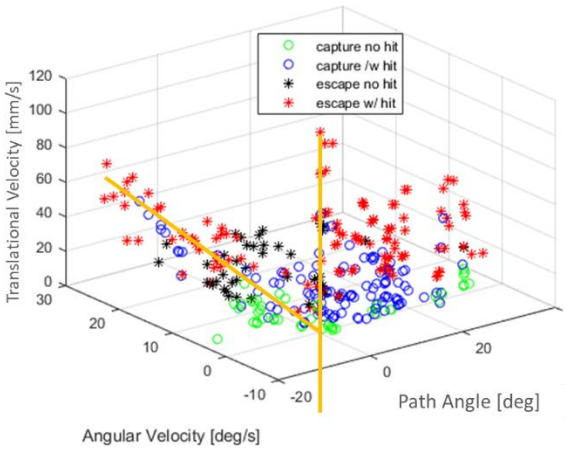

Figure 19. 3D scatter plot with parameters path angle, angular velocity, and translational velocity on the axes. Orange lines represent a path angle of 0 degrees

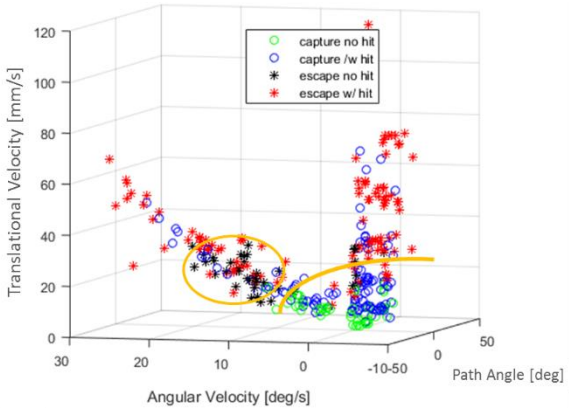

Figure 20. 3D scatter plot with parameters path angle, angular velocity, and translational velocity on the axes for 4 DOF capture and tumble tests. Orange circle includes the region of escapes with collisions and the orange arc bounds the angular velocity and translational velocity for reliable capture

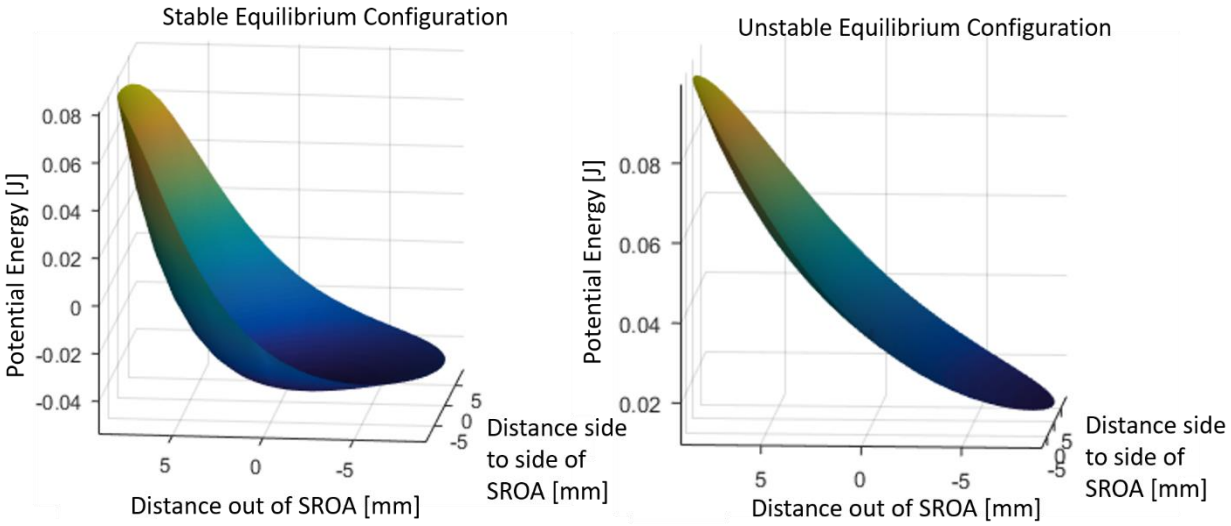

Figure 21. Comparison of a stable and unstable potential wells for different OSA configurations

occur at angular velocities up to either 10 deg/s or 2 cm/s, corresponding to 0.01 J, marked by the orange arc in Figure 20. The capture scenarios with no collisions are a lower energy subset of the larger capture set, with preferential path angles at -10 degrees and 32 degrees, seen in Figure 19. Capture events with collisions occurred much more frequently when the path angle was near 0 deg, with a regime of escapes without collisions separating the lower energy captures with the higher energy captures, as shown by the straight orange lines in Figure 19. This pattern could be the result of the impacts absorbing the rotational kinetic energy of the OSA into an acceptable capture range. The largest occurrence of collision-free escapes happen for a range of angular velocities between 10 deg/s and 20 deg/s, as seen by the orange circle in Figure 20.

The successful capture of tumble tests, shown in Figure 17, depended on angular velocity and the orientation of the OSA upon entering equilibrium position. As seen by the unstable equilibrium potential well (in Figure 21), despite being in equilibrium position, the orientation effects the shape/gradient of the potential well and could reject the OSA. The angle from equilibrium orientation is the combination of roll and yaw displacement, calculated with the differential quaternion. The angular velocity is measured before the OSA enters the potential well. The OSA is more likely to capture when entering the potential well in equilibrium orientation; although for slower velocities, the OSA can be farther skewed from equilibrium orientation and still capture, as shown in Figure 18. The implications for a flight mission are clear: lower relative velocities and angular rates generate more successful, non-impacting capture scenarios. If contact is unacceptable and the OS may experience larger energy states during capture, the state of the OS may need to be estimated to ensure that the OS is within an acceptable range of attitude to guarantee capture.

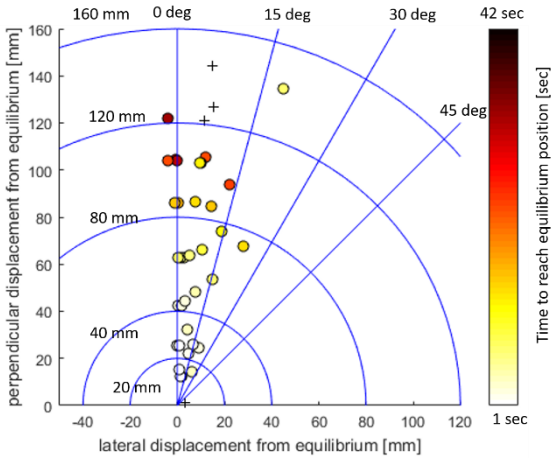

Figure 22. Sphere of influence for different initial displacements for 3DOF system

4.4 Degree of Freedom Sensitivity

By locking the OSA's rotation about the spindle, the FPOS testbed limits the motion to three degrees of freedom. Selected tests and results were repeated in this configuration to investigate the sensitivity of FPI dynamic performance to the number of DOFs available. As can be seen in Figure 22 and Figure 23, the OSA consistently captures at much lower angular and translational velocities, with a corresponding kinetic energy threshold of 0.0025_ as compared to the 0.01 J of the 4DOF system. The 4 DOF tests also showed more subtle effects of the parameters on the system capture state. For example, 4 DOF tests showed that for a zero-degree path angle, captures could be made at higher velocities, but this path angle preference does not appear in the 3 DOF data. Also, most 3 DOF experiments

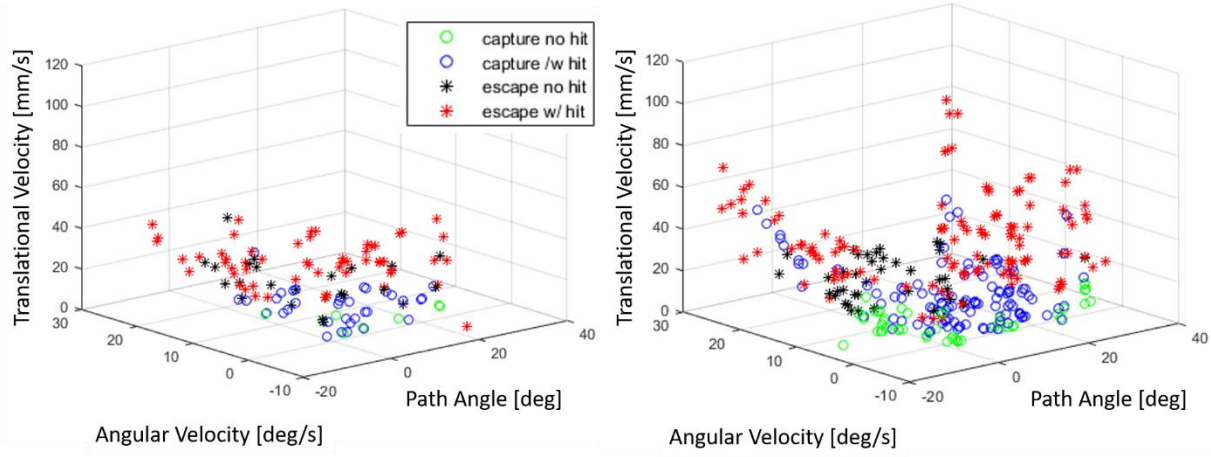

Figure 23: 3D scatter plots showing the reduction in capture range in a 3DOF test (left) from a 4DOF test (right, which is repeated for comparison)

involved collisions. The reason for the reduced performance is likely because the nonlinear degrees of freedom in an FPI are also coupled, so when one degree of freedom is constrained, the energy couples into the remaining degrees of freedom, causing the system to be more likely to exceed the energy thresholds in that particular degree of freedom. However, the sphere of influence (shown in Figure 22) appears to be approximately the same (12 cm). Ultimately, the implications of this sensitivity to the number of degrees of freedom suggest that the best testing environment for an FPI is microgravity – where all six coupled degrees of freedom can be tested simultaneously – but that reduced-degree-of-freedom testbeds can provide conservative, bounding estimates on performance that only improve as the system becomes more flight-like.

5. Conclusion

Flux-pinned interfaces are a unique technology that offer a number of advantages to close-proximity spacecraft maneuvers, including potential sample capture scenarios. For the sample capture concept described in this work, the flux-pinned interface design has been shown to successfully capture an orbiting sample in a four degree-of-freedom ground testbed environment over a variety of conditions. Given the maturity of the cooling system and the 1:1 scale of the FPI dimensions in this testbed, the technology has achieved a system demonstration in a (conservative and bounding) laboratory dynamic environment and a relevant thermal environment.

The results of the test campaigns on the FPOS air-bearing testbed have shown that, for the test hardware, the sphere of influence of the FPI is generally independent of path angle and is about 12 cm in radial distance. This distance is likely to be 50 cm or larger in a Mars environment for a flight-like system. The kinetic energy threshold for capture is approximately 0.01 J, which corresponds to a total relative translational velocity of up to 4.7 cm/sec or a total angular rate of 24 deg/sec between the spacecraft and the sample cache (but not both simultaneously). Achieving better relative approach angles (staying near the 0 degree path angle) may enable those relative bounds to loosen to 16.7 cm/sec or 47 deg/sec for a flight-like system.

Ultimately, however, the FPI's full performance capabilities and dynamic subtleties are not able to be fully expressed in a constrained degree of freedom environment, so these results likely underpredict the performance of a true flight-like system. When the FPOS testbed was constrained to three degrees of freedom, the capture energy threshold was reduced by 80 %, so a full six degree-of-freedom test (whether on a microgravity plane flight [18] or a demonstration in low earth orbit) is the next step in maturing this technology. This information will assist in the tuning of a predictive model for the dynamics that will make it possible to consider FPIs on a potential flight sample-capture mission.

Acknowledgements

This research was in part funded through NSTRF under proposal NNX15AP55H.

This research was carried out at the Jet Propulsion Laboratory, California Institute of Technology, under a contract with the National Aeronautics and Space Administration and funded through the internal Research and Technology Development program.

References

[1] L. Davis, E. Logothetis and R. Soltis, "Stability of Magnets Above Superconductors," *Journal of Applied Physics*, vol. 64, no. 8, pp. 4212-4218, 1988.

[2] J. Hull, "Superconducting Bearings," *Superconducting Science and Technology,* vol. 13, pp. R1-R15, 2000.

[3] P. Ford and G. Saunders, "High-Temperature Superconductivity – Ten Years On," *Contemporary Physics,* vol. 38, no. 1, pp. 63-81, 1997.

[4] M. Norman and M. Peck, "Simplified Model of a Flux-Pinned Spacecraft Formation," *Journal of Guidance, Control, and Dynamics, Vol. 33. No. 3,* pp. 814-822, 2010.

[5] J. Gersch and M. Peck, "Architecting the Very-Large-Aperture Flux-Pinned Space Telescope: A Scalable, Modular Optical Array with High Agility and Passively Stable Orbital Dynamics," in *AS/AIAA Astrodynamics Specialist Conference*, Honolulu, Hawaii, 2008.

[6] J. Shoer, W. Wilson, L. Knobel and M. Peck, "Microgravity Demonstrations of Flux Pinning for Station-Keeping and Reconfiguration of CubeSat-Sized Spacecraft," *Journal of Spacecraft and Rockets,* vol. 47, no. 6, 2010.

[7] L. Jones, W. Wilson and M. Peck, "Design parameters and validation for a non-contacting flux-pinned docking interface," in *AIAA SPACE Conference & Exhibition*, Anaheim, CA, 2010.

[8] M. Sorgenfrei, L. Jones and M. Peck, "Testbed Validation of Location-Scheduled Control of a Reconfigurable Flux-Pinned Spacecraft Formation," *AIAA Journal of Spacecraft and Rockets,* 2013.

[9] W. Wilson, L. Jones and M. Peck, "A Multi-Module Planar Air Bearing Testbed for CubeSat-Scale Spacecraft," *Journal of Dynamic Systems, Measurement and Control,* vol. 135, no. 4, 2013.

[10] L. Jones, W. Wilson, J. Gorsuch, J. Shoer and M. Peck, "Fight Validation of a Multi-Degree-of-Freedom Spacecraft Model," in *AIAA Guidance, Navigation, and Control Conference*, Portland, OR, 2011.

[11] L. Jones and M. Peck, "Control Strategies Utilizing the Physics of Flux-Pinned Interfaces for Spacecraft," in *AIAA Guidance, Navigation, and Control Conference*, Portland, OR, 2011.

[12] M. Norman and M. Peck, "Stationkeeping and Reconfiguration of a Flux-Pinned Satellite Network," in *AIAA Guidance, Navigation, and Control Conference*, Honolulu, Hawaii, 2008.

[13] J. Shoer and M. Peck, "lux-pinned interfaces for the assembly, manipulation, and reconfiguration of modular space systems," *The Journal of the Astronautical Sciences* , vol. 57, no. 3, pp. 667-699, 2009.

[14] J. Shoer and M. Peck, "Sequences of passively stable Dynamic equilibria for hybrid control of reconfigurable spacecraft," in *AIAA Guidance, Navigation, and Control Conference*, Chicago, IL, 2009.

[15] W. Wilson, J. Shoer and M. Peck, "Demonstration of a Magnetic Locking Flux-Pinned Revolute Joint for Use on CubeSat-Standard Spacecraft," in *AIAA Guidance, Navigation, and Control Conference*, Chicago, IL, 2009.

[16] J. Shoer and M. Peck, "Reconfigurable spacecraft as kinematic mechanisms based on flux-pinning interactions," *Journal of Spacecraft and Rockets,* vol. 46, no. 2, pp. 466-469, 2009.

[17] J. Doebbler, J. J. Davis, J. Valasek and J. L. Junkins, "Mobile Robotic System for Ground Testing of Multi-Spacecraft Proximity Operations," in *AIAA Modeling and Simulation Technologies Conference and Exhibit*, Honolulu, HI, 2008.

[18] R. Kornfield, J. Parrish and S. Sell, "Mars Sample Return: Testing the Last Meter of Rendezvous and Capture," *Journal of Spacecraft and Rockets,* vol. 44, no. 3, pp. 692-700, 2007.

[19] J. Pei, L. Murchison, A. BenShabat, V. Stewart, R. Elandt, D. Elliott and A. Weber, "Autonomous Rendezvous and Docking of Two 3U Cubesats Using a Novel Permanent-Magnet Docking Mechanism," in *54th AIAA Aerospace Sciences Meeting* , San Diego, 2016.

[20] F. Zhu, L. Jones-Wilson, W. Jones-Wilson, T. Burney and M. Peck, "A 4 degree of freedom air bearing small satellite simulator for dynamics and controls," vol. In progress., 2016.

[21] I. M. McKinley and L. L. Jones-Wilson, "A Flight-Traceable Cryogenic Thermal System for use in a Sample-Capture Flux-Pinned Interface," *Cryogenics,* 2016.

[22] H. C. Schubert and J. P. How, "Space Construction: an Experimental test bed to Develop Enabling Technologies," *Intelligent Systems & Advanced Manufacturing,* pp. 179-188, 1997.

[23] D. Sternberg, C. Pong, N. Filipe, S. Mohan, S. Johnson and L. Jones-Wilson, "JPL Small

Satellite Dynamics Validation: Validated Models for Predicting On-Orbit Performance," *Journal of Guidance, Navigation, and Control*, 2017.

[24] A. Kordyuk, "Magnetic levitation for hard superconductors," *Journal of Aplied Physics*, vol. 83, no. 1, pp. 610-612, 1998.

[25] D. Villani, "An analytic solution for the force between two magnetic dipoles," *Magnetic and Electrical Separation* , vol. 9, pp. 39-52, 1998.

[26] P. Landecker, D. Villani and K. Yung, "An analytic solution for the torque between two magnetic dipoles," *Physical Separation in Science and Engineering* , vol. 10, no. 1, pp. 29-33, 1999.

[27] F. Zhu, L. Jones-Wilson, W. Jones-Wilson, T. Burney and M. Peck, "A 4 degree of freedom air bearing small satellite simulator for dynamics and controls," *In Progress.*